ACS APPLIED NANO MATERIALS

www.acsanm.org

Article

Hardening of Cobalt Ferrite Nanoparticles by Local Crystal Strain Release: Implications for Rare Earth Free Magnets

Beatrice Muzzi, Elisabetta Lottini, Nader Yaacoub, Davide Peddis, Giovanni Bertoni, César de Julián Fernández, Claudio Sangregorio,* and Alberto López-Ortega*

Cite This: *ACS Appl. Nano Mater.* 2022, 5, 14871−14881

Read Online

ACCESS | Metrics & More | Article Recommendations | Supporting Information

ABSTRACT: In this work, we demonstrate that the reduction of the local internal stress by a low-temperature solvent-mediated thermal treatment is an effective post-treatment tool for magnetic hardening of chemically synthesized nanoparticles. As a case study, we used nonstoichiometric cobalt ferrite particles of an average size of 32(8) nm synthesized by thermal decomposition, which were further subjected to solvent-mediated annealing at variable temperatures between 150 and 320 °C in an inert atmosphere. The postsynthesis treatment produces a 50% increase of the coercive field, without affecting neither the remanence ratio nor the spontaneous magnetization. As a consequence, the energy product and the magnetic energy storage capability, key features for applications as permanent magnets and magnetic hyperthermia, can be increased by ca. 70%. A deep structural, morphological, chemical, and magnetic characterization reveals that the mechanism governing the coercive field improvement is the reduction of the concomitant internal stresses induced by the low-temperature annealing postsynthesis treatment. Furthermore, we show that the medium where the mild annealing process occurs is essential to control the final properties of the nanoparticles because the classical annealing procedure (T > 350 °C) performed on a dried powder does not allow the release of the lattice stress, leading to the reduction of the initial coercive field. The strategy here proposed, therefore, constitutes a method to improve the magnetic properties of nanoparticles, which can be particularly appealing for those materials, as is the case of cobalt ferrite, currently investigated as building blocks for the development of rare-earth free permanent magnets.

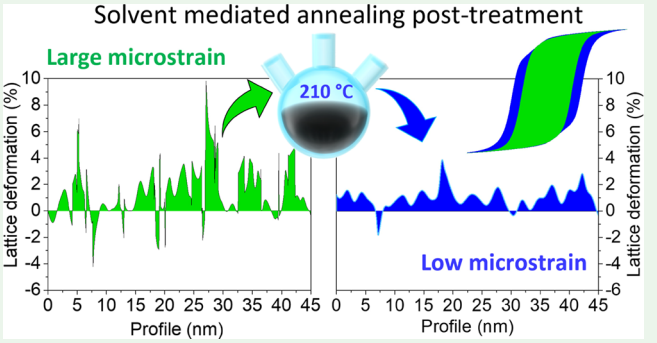

KEYWORDS: *cobalt ferrite, magnetic nanoparticles, microstrain, geometrical phase analysis, solvent-mediated annealing, coercivity*

INTRODUCTION

Magnetic anisotropy and coercive force are key properties of magnetic materials, which, together with remanence and saturation magnetization, define their applicability in many technologies, such as magnetic hyperthermia, data storage, and permanent magnets.[1−3] The reduction of the size down to the nanoscale is a well-established approach for the improvement of these properties in many traditional magnetic materials, such as spinel ferrites, hexagonal ferrites, or metal alloys.[4−6] Matter at the nanoscale, indeed, exhibits exotic morphologies, structures, and properties which are intrinsically correlated with their metastable nature and arise from the different competitive and intertwined energy contributions coming from the dominant surface, size effects, the composition, and the chemical state.

Accordingly, the demanding requirements of technological applications have fueled the search for suitable strategies to improve the magnetic properties by fine controlling the morpho-structural features. In this framework, iron-based oxides, such as spinel ferrites or hexagonal ferrites, have demonstrated their high magnetic versatility through the control of their composition as well as of their shape and size.[7,8] In addition, an extra degree of freedom is provided by the combination of diverse iron-based magnetic phases in exchange-coupled bi-magnetic nanosystems.[9,10] Nevertheless, most of these strategies must cope with the intrinsic defectiveness which characterizes nanomaterials, arising from the constraints imposed during the synthesis to limit their growth to the nanoscale. Most of the studies reported so far focus on the modification of the surface of the nanoparticles (NPs) through reconstruction of the spin disordered shell,[11,12] the increase of the surface anisotropy contribution,[13−15] or by exchange-coupling.[16−18] More recently, attention has focused

Received: July 19, 2022
Accepted: September 1, 2022
Published: September 21, 2022

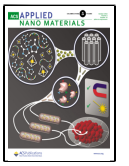

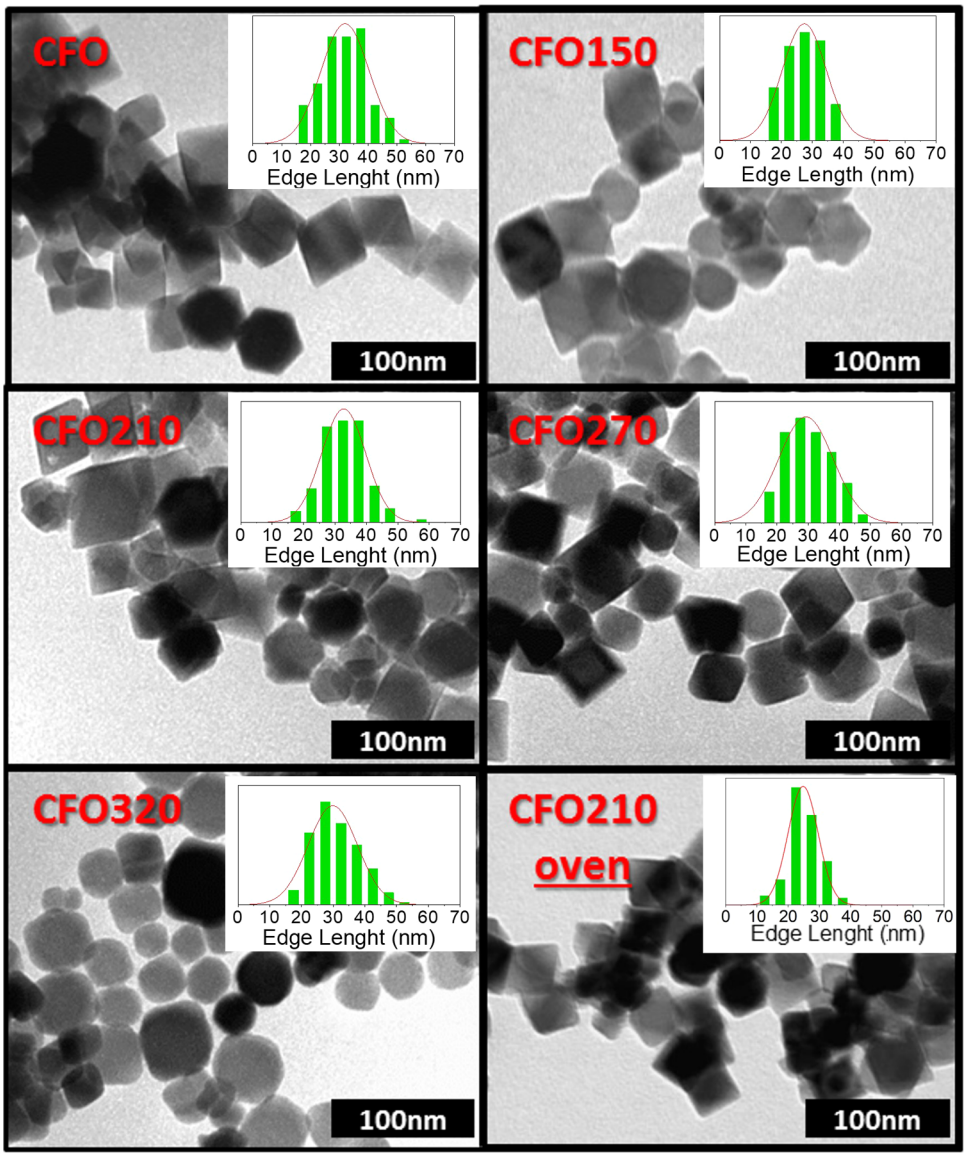

Figure 1. Selected TEM images and corresponding particle edge length histograms for as-prepared and annealed nanoparticles.

also on the core spin structure.[19] As an example, the synthesis of defect-engineered iron oxide NPs has been shown to be effective in boosting the hyperthermic efficiency of iron oxide NPs,[20] as well as the permanent magnet properties in cobalt ferrite particles.[21] Local distortions of the ligand field, dislocations, vacancies, antiphase boundaries, or the coordination distortions at the surface sites can indeed drastically affect the magnetic anisotropy of the final material.[21−23]

Thermal treatment is a conventional strategy to tailor the properties of the NPs, driving them to the minimum free energy configuration by extended changes of their morphological and chemical−physical properties through thermally driven atomic diffusions, crystal reconstruction, and shape modifications. However, the annealing can give rise to nucleation and growth of the particles, favoring the interparticle aggregation, reduction of the lattice defects, and charge-cation changes, mainly when air annealing is performed.[24] Because all these effects are size-dependent and strongly intertwined, the tailoring of individual properties, such as the magnetic anisotropy, while keeping other structural and magnetic properties unaltered, is hard to be achieved.

Conversely, here, we demonstrate how choosing a mild thermal solvent mediated annealing, it is possible to release the internal stress without affecting the lattice defects, leading to an unprecedent final increase of the total magnetic anisotropy, without affecting any other structural or magnetic parameter (neither saturation, nor remanence magnetization). The validity of such an approach has been proved on cobalt ferrite ($Co_xFe_{3-x}O_4$) NPs of ∼30 nm prepared by thermal decomposition in benzyl ether. Cobalt ferrite is particularly suited to this aim because of its large cubic magneto-crystalline anisotropy, which is responsible for its high H_C, the moderately high saturation magnetization, the large magnetostriction, high stability,[25,26] and the easiness of preparation in the form of NPs with a controlled size and shape.[8]

The analysis of the effect of the solvent-mediated annealing at variable temperatures between 150 and 320 °C on the structural and magnetic properties clearly shows that, when low temperatures are considered (up to 210 °C) the thermal treatment causes the reduction of the nonuniform crystal lattice microstrain accumulated during the NP growth, increasing the H_C, the energy product $(BH)_{max}$, and the total

https://doi.org/10.1021/acsanm.2c03161
ACS Appl. Nano Mater. 2022, 5, 14871−14881

Table 1. Summary of the Annealing Temperature and Structural Data Obtained from TEM and XRD Analyses[a]

samples	annealing temperature (°C)	TEM	XRD		
		l (nm)	a (nm)	microstrain	crystal size (nm)
CFO		33(2)	0.8398(1)	7.0×10^{-4}	45(2)
CFO150	$150^{(sol.)}$	29(2)	0.8404(1)	1.3×10^{-5}	41(2)
CFO210	$210^{(sol.)}$	33(2)	0.8406(1)	4.9×10^{-7}	41(2)
CFO270	$270^{(sol.)}$	29(6)	0.8404(1)	4.7×10^{-6}	40(2)
CFO320	$320^{(sol.)}$	30(2)	0.8401(1)	2.3×10^{-4}	40(2)
CFO210-oven	$210^{(pow.)}$	27(2)	0.8403(1)	1.0×10^{-3}	40(2)

[a]TEM particle size was assessed by considering the edge length of cubes or octahedrons (l) and fitting the distribution to a lognormal function. a refers to the cell parameter for the cubic spinel structure. Lattice parameter, microstrain, and crystal size are obtained by Rietveld refinement of the experimental patterns. Uncertainties on the last digit are given in parentheses. Note that the error for microstrain has been assessed to the 10% of the calculated value.

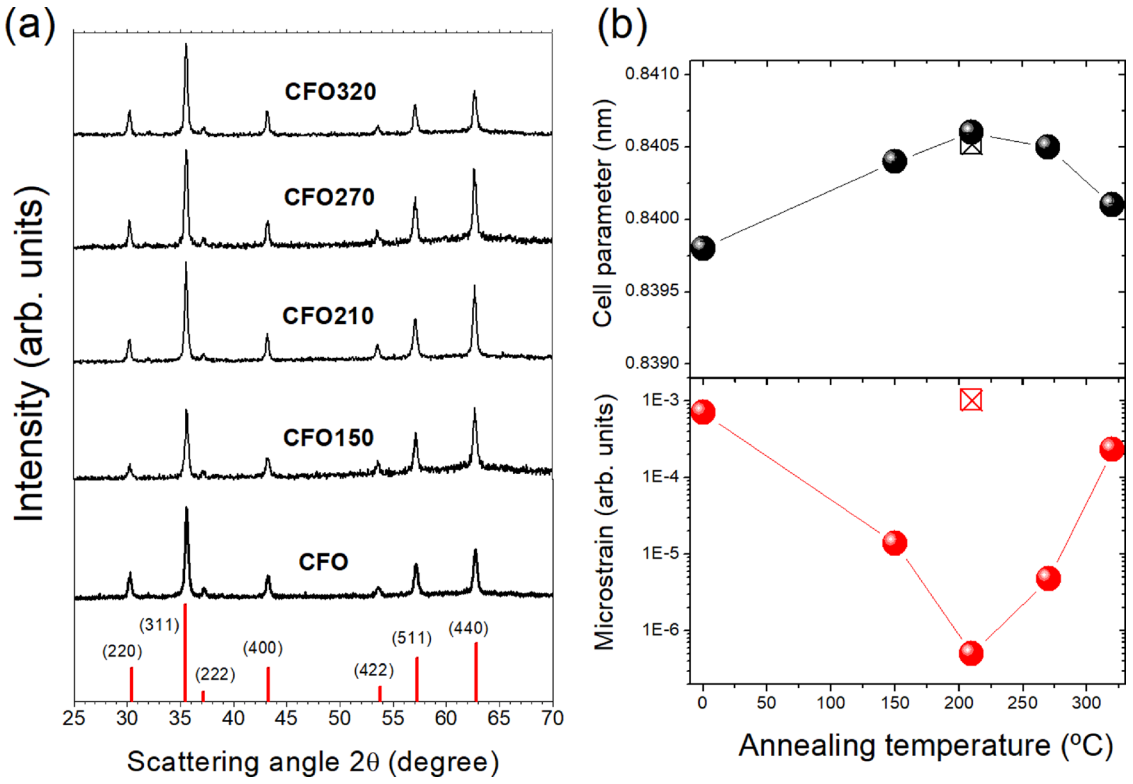

Figure 2. (a) XRD patterns for the as-prepared and annealed cobalt ferrite NPs (red bars refer to the position of the diffraction peaks for the cobalt ferrite crystal structure). (b) Cell parameter (top) and microstrain (bottom) dependence on the annealing temperature (black ballot box with X and red ballot box with X refer to the **CFO210-oven** sample). Error bars are not visible because they are smaller than symbols.

magnetic energy of the nanomaterial. Moreover, we prove the crucial role of the solvent, compared to classical annealing procedures, to induce the effect.

RESULTS AND DISCUSSION

Octahedral ferrite NPs of composition $Co_{0.4}Fe_{2.6}O_4$, as determined by energy-dispersive X-ray fluorescence (EDXRF) analysis (Supporting Information, Table S1), with average edge size, l, of 32(8) nm and narrow particle size distribution (σ < 20%), were synthesized by thermal decomposition of metal−organic precursors in the high-boiling point solvent benzyl ether, as described in ref 8 (sample **CFO**). Afterward, the as-prepared NPs were dispersed in high boiling solvents (benzyl ether or octadecene) with the help of oleylamine (OAm) and oleic acid (OA) as surfactants and annealed under an inert atmosphere at different temperatures, 150, 210, 270, and 320 °C. In the following, the samples will be denoted as **CFO#** where # corresponds to the annealing temperature. In addition, a fraction of the as-prepared sample was annealed in an oven at 210 °C under an inert atmosphere, to compare the effect of the heating media in the thermal treatment (sample **CFO210-oven**).

Figure 1 depicts representative bright-field, low-magnification, transmission electron microscopy (TEM) images of the as-prepared and annealed NPs, with the corresponding particle size histograms. **CFO** comprises octahedral shaped particles, as expected for cobalt ferrite grains larger than 20 nm.[27] The annealing process does not modify the particle size nor the size distribution of the system, which maintains a narrow deviation, lower than 20% (see Table 1). Moreover, the thermal treatment does not have any effect on the shape of the NPs when the heating temperature is increased up to 270 °C, independently of the heating process used (oven or solvent mediated annealing). Conversely, at higher temperatures (320

https://doi.org/10.1021/acsanm.2c03161
ACS Appl. Nano Mater. 2022, 5, 14871−14881

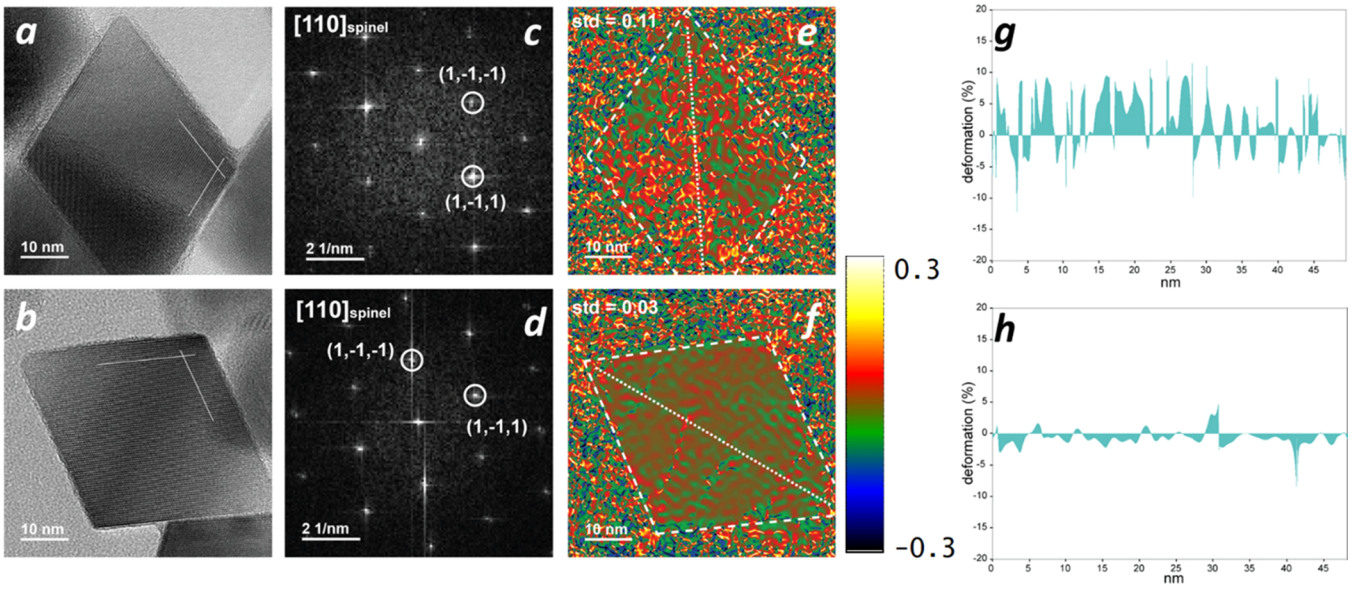

Figure 3. HRTEM images of a (a) **CFO** and a (b) **CFO210** NPs with FFT analysis (c,d) obtained from the NP in (a) and (b), respectively. The labeled spots are related to crystallographic planes that can be indexed as cubic spinel structure ($Fd\bar{3}m$), in zone axis [110]. Strain maps ϵ_{xy} (symmetric shear) obtained by GPA analysis of the NPs (e) before and (f) after thermal annealing. The maps are calculated from (e,f) g_1 = (1-1-1) and g_2 = (1-11) reflections respectively, and plotted in the relative interval (−0.3, +0.3). Lattice deformation percentage profiles of (g) **CFO** and (h) **CFO210** measured along the diagonal of the NP (dotted white line), which allowed to estimate the relative displacement of the (111) planes with respect to the reference region (see the SI for further details).

°C) the thermal process has a smoothing effect on particle edges changing the NP shape in truncated octahedrons or cubes. Such modification can be easily explained by the higher reactivity of the NP corners, which are the first part of the crystal affected by Ostwald ripening, induced by the relatively high temperatures used in the annealing process.[28]

High-resolution TEM (HRTEM) investigations performed on **CFO** and **CFO210** (see Supporting Information, Figure S1) confirmed that the two samples share the same morphology (octahedral shape) and have a highly ordered crystal structure along the entire NP. The detailed analysis of the fast Fourier transform (FFT) images revealed that the characteristic spots for the cobalt ferrite structure, observed in the as-prepared sample, **CFO**, are preserved after the annealing process (see Supporting Information, Figure S1). Finally, EDXRF measurements proved that the stoichiometry of the pristine sample ($Co_{0.4}Fe_{2.6}O_4$) is maintained for all the samples, and thus no metal ion leaking occurs during the heating (Supporting Information, Table S1).

The X-ray diffraction (XRD) patterns indicate the presence of a single crystallographic phase (Figures 2a and S2), indexed to a cubic spinel structure (space group $Fd\bar{3}m$, JCPDS PDF #221086). The calculated crystal size is consistent with that obtained from TEM images, indicating the growth of highly ordered single-crystal structures (Table 1). The cell parameter, *a*, for all the series of samples is in the range expected for nonstoichiometric cobalt ferrite, that is, $Co_{0.4}Fe_{2.6}O_4$;[27,29] however, as the annealing temperature is increased a nonmonotonic dependence is observed with a maximum for the sample annealed at 210 °C (**CFO210**). An opposite trend is displayed by the microstrain, estimated from the Rietveld analysis of the experimental pattern, although in this case the percentage change is much more pronounced (Figure 2b and Table 1) spanning three orders of magnitude between **CFO**, 7.0×10^{-4}, and **CFO210**, 4.9×10^{-7}. Both trends can be explained by the reduction of internal stresses created during the growth of the NPs, considering that a microstrain value below 1×10^{-5} indicates its quasi-complete disappearance.

The annealing treatment, indeed, permits the reduction of the intrinsic plastic deformations created during the growth of the nanocrystallites. These deformations are responsible for local distortion of lattice planes that gives rise to a nonuniform variation in the interplanar distances (i.e., microstrain).[30] As the annealing temperature is increased, a progressively larger partial release of internal stress occurs, reducing the associated strain. However, when the temperature reaches 270 °C, the increased reactivity of the system in the annealing medium can slightly affect the cationic homogeneity along the NPs, modifying the cell parameter, with a consequent increase of the strain in the nanostructure.[31,32] On the other hand, the sample annealed at 210 °C in the oven (**CFO210-oven**) has cell parameter and crystal size values consistent with those obtained for the solvent-mediated annealed samples, but the calculated microstrain is much larger. The different heating treatment environment has thus a different effect on the capability of the NPs of releasing the stress.

These results are nicely supported by local analysis performed on a single NP (Figure 3) by geometrical phase analysis (GPA).[33] The comparison between **CFO** and **CFO210** highlights that, after the thermal treatment, the displacement of the crystallographic planes in the 3D lattice is reduced. The strain maps were calculated for the (002) and (111) reflections (Figure S1) to estimate the displacement of these planes from their reference (i.e., average) positions in the spinel structure. The strain mapping clearly shows that after thermal annealing the lattice strain significantly decreases in comparison with the as-prepared samples, the lattice deformation being less than ca. 2% for sample **CFO210** (Figure 3f). Conversely, no significant changes were distinguished for the (002) crystallographic plane before and after thermal treatment. Thus, the disorder in the as-prepared MNPs originates mainly from (111) planes in **CFO**, and then

https://doi.org/10.1021/acsanm.2c03161
ACS Appl. Nano Mater. 2022, 5, 14871−14881

it is mitigated by the thermal treatment in **CFO210** (see the Supporting Information for more details).

To investigate the evolution of the magnetic structure with the annealing temperature, ^{57}Fe Mössbauer spectra under intense magnetic field (8 T) were recorded at 12 K on selected samples **CFO**, **CFO210**, and **CFO320** (Figure 4). For some details on the technique and on the fitting of spectra see the Supporting Information. The in-field spectra of the different samples are split into two main sub-spectra corresponding to the iron ions located at tetrahedral (A) and octahedral (B) sites, respectively.

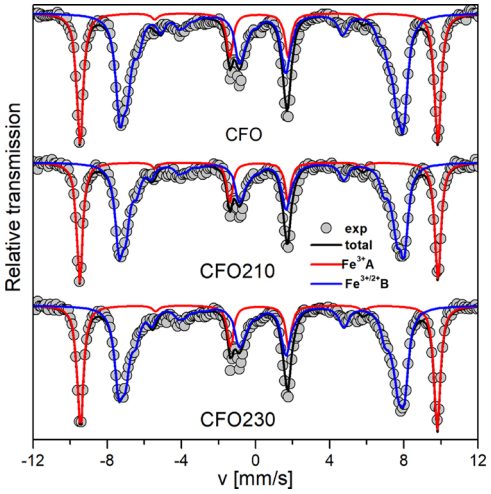

Figure 4. Mössbauer spectra measured at 12 K under 8 T magnetic field for **CFO**, **CFO210**, and **CFO320**. Gray dots and black solid lines are experimental and simulated total spectrum. Red and blue lines are the simulated sub-spectrum corresponding to A and B sites, respectively. Detailed fit of A and B sites is reported in the Supporting Information (Figure S3).

It should be noted that while the refined values of the mean isomer shift, δ, (Table 2) correspond to those expected for Fe^{3+} in the A-site for the cobalt ferrite structure, slightly higher values are observed in B-sites, indicating the presence of some Fe^{2+}. The presence of divalent iron cations has been also confirmed by the mean refined value of the hyperfine field, B_{hyf}, which are lower than those of stoichiometric cobalt ferrite.[34−36] The relative population of Fe in A and B sites is equal within the experimental error for all the samples, indicating that thermal treatment does not affect cation distribution.[34,37,38] Moreover, the nonzero intensity contribution clearly indicates the presence of a noncollinear spin structure, showing a mean canting angle that, within the experimental error, is equal for all the samples.[38−40]

The magnetic properties of the samples were investigated by measuring the hysteresis loop at 5 and 300 K. Low-temperature measurements (Figures 5 and S4) performed after a field cooling procedure show that the pristine material has $\mu_0 H_C$ of ∼1.5 T, a specific saturation magnetization value at 5 T (M_{5T}) of ∼80 Am^2 kg^{-1}, and a reduced remanence value ($R = M_R/M_{5T}$) of 0.83 (Table 3). These values are in agreement with those expected for an assembly of randomly oriented, nonstoichiometric cobalt ferrite NPs of roughly 30 nm.[8,26,29] Moreover, the comparison of the loops of the various samples demonstrates that the annealing procedure does not affect neither the saturation magnetization of the system nor the reduced remanence. This result confirms that thermal treatment does not force internal chemical reactions or large modifications of the crystal and spin structures of the system, as indeed already indicated by XRD and Mössbauer experiments. Conversely, the coercive field is largely modified by the annealing procedure and exhibits a nonmonotonic behavior with a maximum for **CFO210** corresponding to 2.12 and 0.19 T for 5 and 300 K, respectively, (Figure 5b), which is ca. 60% larger than **CFO**.

Interestingly, the $\mu_0 H_C$ trend well reproduces that observed for the cell parameter and microstrain. Therefore, by considering that neither chemical nor structural modifications occurred during the annealing, it can be argued that it is the reduction of the internal strain in the NPs that leads to a net increase of the coercivity of the sample. This behavior is contrary to that previously reported for submicron cobalt ferrite particles prepared by a ball-milling process,[41−44] where the strong energy generated during the milling causes the proliferation of structural defects generating stress-induced anisotropy and pinning centers for domain wall motion, which increase H_C.[44] However, in the present case, thanks to the high crystallinity of the NPs the presence of this kind of stress anisotropy can be neglected. Moreover, the nanometric dimension of the NPs allows for excluding the presence of domain-wall driven switching, so that pinning centers cannot determine the magnetization dynamics of the system.[8,45]

Any attempt to rationalize this unexpected behavior requires taking into account the magneto-elastic energy, which adds a contribution to the total magnetic energy that, in a single domain particle, determines the reversal dynamics and the coercive field (inverse magnetostrictive effect).[46−48] In the framework of the Stoner−Wohlfarth model, a strain, ε, induces, in random oriented particles, an additional uniaxial magnetic anisotropy, characterized by the magneto-elastic anisotropy constant, $K_{elas} = 3/2\lambda_s\varepsilon$, where λ_s is the magneto-

Table 2. Mean Isomer Shift (δ), Mean Quadrupole Shift (2ε), Mean Hyperfine Field (B_{hyf}), Mean Canting Angle (θ), and Relative Amount of Fe in A and B Cavities Evaluated from Fitting In-Field Mössbauer Spectra Are Reported for Samples CFO, CFO210, and CFO320[a]

sample	site	δ (mm s^{-1})	2ε (mm s^{-1})	B_{hyf} (T)	θ (°)	$Fe_{A,B}/Fe_{total}$
CFO	Fe^{3+}_A	0.36(1)	−0.00(1)	52.0(2)	15	0.34(1)
	$Fe^{3+/2+}_B$	0.60(1)	−0.11(1)	51.2(2)	24	0.66(1)
CFO210	Fe^{3+}_A	0.35(1)	−0.00(1)	52.0(2)	14	0.34(1)
	$Fe^{3+/2+}_B$	0.60(1)	−0.15(1)	51.6(2)	23	0.66(1)
CFO320	Fe^{3+}_A	0.35(1)	−0.00(1)	51.8(2)	15	0.34(1)
	$Fe^{3+/2+}_B$	0.60(1)	−0.12(1)	51.2(2)	25	0.66(1)

[a]Uncertainties on the last digit are given in parentheses and the error for canting angle has been assessed to be 10°.

https://doi.org/10.1021/acsanm.2c03161
ACS Appl. Nano Mater. 2022, 5, 14871−14881

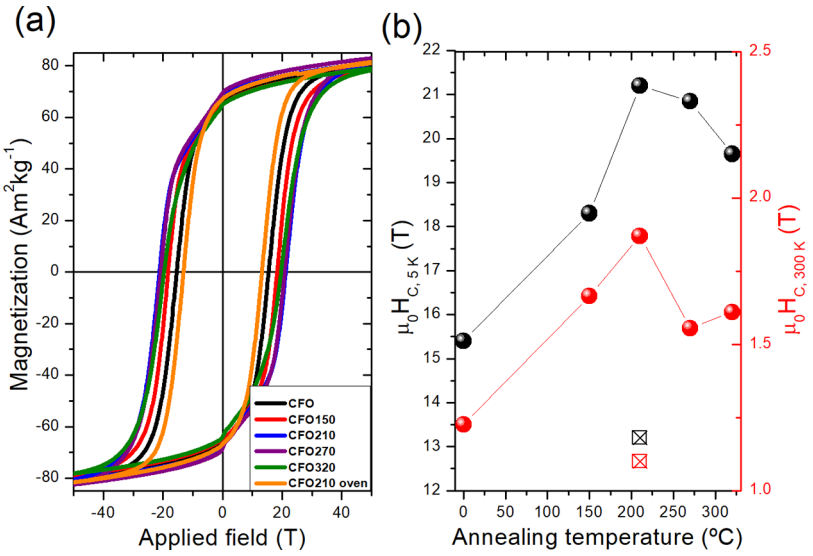

Figure 5. (a) Hysteresis loops for the as-prepared and annealed cobalt ferrite NPs measured at 5 K; (b) coercive field ($\mu_0 H_C$) dependence measured at 5 K (black) and 300 K (red) as a function of the annealing temperature (black ballot box with X and red ballot box with X refer to **CFO210-oven**).

Table 3. Magnetic Properties of Cobalt Ferrite NPs Measured at 5 and 300 K: $\mu_0 H_C$ Coercive Field, R Reduced Remanence, M_{5T} Specific Saturation Magnetization at 5 T, M_S Extrapolated Saturation Magnetization, K_{eff} Effective Magnetic Anisotropy, and $(BH)_{max}$ Room-Temperature Energy Product[a]

	5 K					300 K			
samples	$\mu_0 H_C$ (T)	R	M_{5T} (Am^2 kg^{-1})	M_S (Am^2 kg^{-1})	K_{eff} (MJ m^{-3})	$\mu_0 H_C$ (T)	R	M_{5T} (Am^2 kg^{-1})	$(BH)_{max,\ 300\ K}$ (kJ m^{-3})
CFO	1.54	0.83	80	84	1.01	0.12	0.34	78	7.2
CFO150	1.83	0.82	79	83	1.23	0.17	0.48	78	8.8
CFO210	2.12	0.84	81	84	1.39	0.19	0.49	79	12.7
CFO270	2.09	0.84	83	86	1.35	0.16	0.48	80	12.0
CFO320	1.96	0.82	79	82	1.28	0.16	0.46	77	10.4
CFO210-oven	1.32	0.83	82	85	0.83	0.11	0.34	79	5.6

[a]Uncertainties on the last digit are given in parentheses. The errors for M_S, M_{5T}, and $\mu_0 H_C$ have been assessed to be the 5 and 2%, respectively, of the experimental values.

elastic constant. Because bulk cobalt ferrite has a cubic anisotropy and it is an anisotropic magneto-elastic material, λ_s should be written as $\lambda_s = 1/5\ (2\lambda_{100} + 3\lambda_{111})$, where λ_{100} and λ_{111} are the magnetoelastic constant along the <100> and <111> directions. We can first consider the effect of the stress release associated with the variation of the lattice parameter, $\sigma = (a_{CFO210} - a_{CFO})/a_{CFO} = +9 \times 10^{-4}$, where a_{CFO} and a_{CFO210} denote the cubic edge of the unit cell of **CFO** and **CFO210**, respectively, and the latter sample is assumed to have no residual strain ($\varepsilon = 0$). The equivalent strain ε is given by $\varepsilon = E\sigma$ where E is Young's modulus. Considering the values for E and λ_s reported in the literature for cobalt ferrite ($E = 1.4 \times 10^{11}$ N m^{-2}, $\lambda_{100} = -425 \times 10^{-6}$, and $\lambda_{111} = +163.7 \times 10^{-6}$)[49,50] and the experimental lattice parameter variation, we obtain $K_{elas} = -1.4 \times 10^4$ J m^{-3}. This value is largely overestimated because it refers to a unidirectional strain, while the lattice variation is isotropic. Nevertheless, independent of its magnitude, K_{elas} provides a negative contribution along the same directions of the magneto-crystalline anisotropy (we remind that cobalt ferrite has positive cubic magneto-crystalline anisotropy, which makes the easy axes to lie along the <100> directions). Therefore, if this were the dominant term, the coercivity of **CFO** would be larger than that of **CFO210**, which is not the case.

On the other hand, the structural characterization evidenced that the release of microstrain occurs preferentially along the {111} planes. This microstrain is responsible of compressions and expansions of the interplanar distance with respect to the average value, which is also confirmed by the GPA maps and lattice deformation profiles. This positive and negative local strain will differently affect the energy profile for the reversal of the magnetization, creating exchange coupled regions where the local magnetic anisotropy is higher and others where it is lower than the unstrained sample. As an example, if fluctuations $\varepsilon = \pm 7 \times 10^{-4}$ along the <111> directions are considered, an additional contribution to the local magnetic anisotropy energy of $\mp 2.2 \times 10^3$ J m^{-3} is obtained, which is large enough to modify the reversal process of the magnetization (the bulk magneto-crystalline anisotropy is in fact 5×10^4 J m^{-3}). Moreover, lattice deformation profiles suggest that local lattice parameter fluctuations in the {111} planes are much higher than the average value obtained by XRD analysis used for this rough estimation (even larger than K_{elas} value previously evaluated). Therefore, strong magnetic anisotropy local fluctuations will be likely to occur in **CFO**, which can favor incoherent magnetization reversal mechanisms into the particles. These latter are characterized by a lower energy barrier than the pure coherent rotation process, which is presumably operative in **CFO210**, reducing the coercivity of

https://doi.org/10.1021/acsanm.2c03161
ACS Appl. Nano Mater. 2022, 5, 14871−14881

the material. We can thus conclude that in the case of our single-domain cobalt ferrite NPs the improvement of the magnetic properties is driven by the reduction of the internal strains and of the nonuniform variations in the interplanar distances inside the NPs.

To further evidence the impact of the thermal treatment on the magnetic properties, the maximum energy product (BH_{max}) at RT, which is the figure of merit of a permanent magnet, is calculated as a function of the annealing temperature (see Figure 6).[51] BH_{max} is 7.2 kJ m^{-3} for **CFO** and then it varies with

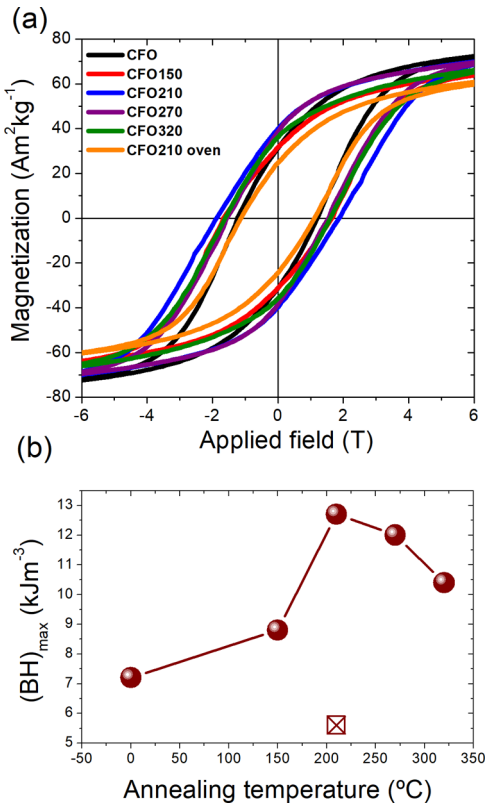

Figure 6. (a) Hysteresis loops for the as-prepared and annealed cobalt ferrite NPs measured at 300 K (enlargement of the low field region). (b) $(BH)_{max}$ product as a function of the annealing temperature (black ballot box with X refers to the **CFO210-oven** sample).

the thermal treatment temperature following the same nonmonotonic trend observed for the coercive field, with a maximum increase of more than 70% for **CFO210** (12.7 kJ m^{-3}). Similarly, magnetic losses, which also depend on the area of the BH hysteresis loop, increase by the same percentage, from 131 kJ m^{-3} for **CFO** to 226 kJ m^{-3} for **CFO210,** respectively. This energy can be released as thermal energy after a complete hysteresis loop is completed, and thus, it defines the performance of the material as heat mediators in key technologies as tumor therapy by magnetic fluid hyperthermia[52−55] and magnetic induction catalysis.[56−59] These results further confirm that a controlled annealing procedure in a solvent-mediated medium allows for improving the capability of this material of storing energy.

It should be stressed that the described modification of NPs' magnetic anisotropy is not simply related to a temperature effect, but also depends on the NP environment state (solid or liquid) where the heating process is carried out. As reported in Table 3 and Figure 5, indeed, when dried **CFO** cobalt ferrite NPs are annealed in an oven at 210 °C (**CFO210-oven**), they exhibit a reduced coercivity, not only with respect to NPs annealed at the same temperature in solvent (**CFO210**) but also to the starting sample. This effect can be attributed to the different NPs' surface−surfactant interaction, which characterizes the two processes. Indeed, in a solid−liquid system, such as that of the solvent-mediated annealing, the surfactant adsorption is a dynamic equilibrium where the molecules are perpetually arriving at and leaving the surface.[60] Thus, during the solvent-mediated annealing, the NPs' surface is partially free to reduce the lattice strain with a decrease of the planes' deformation percentage (Figures 4 and S1). Conversely, in the case of the oven-annealed powder, the organic capping layer forms a very stable thin layer around the NPs, which can hamper the complete release of the accumulated stress.[30] On the other hand, the presence of a thin capping layer can also modify the NPs' interactions. Indeed, ΔM_{plots} (Figure S5 in the SI) performed on **CFO**, **CFO210**, **CFO320**, and **CFO210-oven** have shown for all the samples a prevalence of demagnetizing (i.e., dipolar) interactions. **CFO**, **CFO210**, and **CF320** show comparable interactions strength, with an increase of ΔM field corresponding to the increase of MNPs' magnetic anisotropy. Conversely, an evident increase of interparticle interaction strength had been observed in **CFO210-oven**.

Finally, it is worth stressing that the observed behavior is not occasional. To confirm the reproducibility of the methodology herein presented, another set of cobalt ferrite NPs (**CFO_2_#**), with average edge size, *l*, of 43(5) nm, was subjected to controlled solvent annealing treatment at variable temperature (Supporting Information, Figure S6). Even for **CFO_2_#** a net increase of the coercive field was observed for the NPs annealed in solution with a maximum at 210 °C. This result confirms that the solvent-mediated annealing is an effective and reliable pathway to control the magnetic properties of NPs, through the release of internal structural stress of the particles.

CONCLUSIONS

The thermal decomposition approach has been proposed in the literature as an efficient route to prepare cobalt ferrite NPs with high-energy products. Nevertheless, although at a first sight this technique provides magnetic nanostructures exhibiting high structural and spin arrangement orders, we here demonstrated that postsynthesis mild treatment at controlled low temperature can be effective to significantly improve the energy product of the material. We indeed found that a solvent-mediated annealing treatment in mild conditions (ca. 200−300 °C) permits the reduction of the internal stresses generated during the nanocrystal growth, without affecting neither the morphology, nor the chemical composition, or the structure of the NPs.

A deep structural investigation pointed out that the as-prepared cobalt ferrite NPs display anisotropic lattice strain, the family planes passing through the tetrahedral sites, that is, {111}, being characterized by the highest lattice deformations. These local deformations produce fluctuations of the energy barrier for the magnetization reversal, favoring the onset of incoherent reversal processes. The solvent-mediated annealing treatment allows the release of the local internal strain and fosters the restoring of a pure coherent reversal process. Because the latter is associated with a higher energy barrier, the coercive field increases, being up to 50% higher than in the

https://doi.org/10.1021/acsanm.2c03161
ACS Appl. Nano Mater. 2022, 5, 14871−14881

Scheme 1. Schematic Representation of the Cobalt Ferrite Nanoparticle Synthesis and the Posterior Solvent-Mediated Annealing

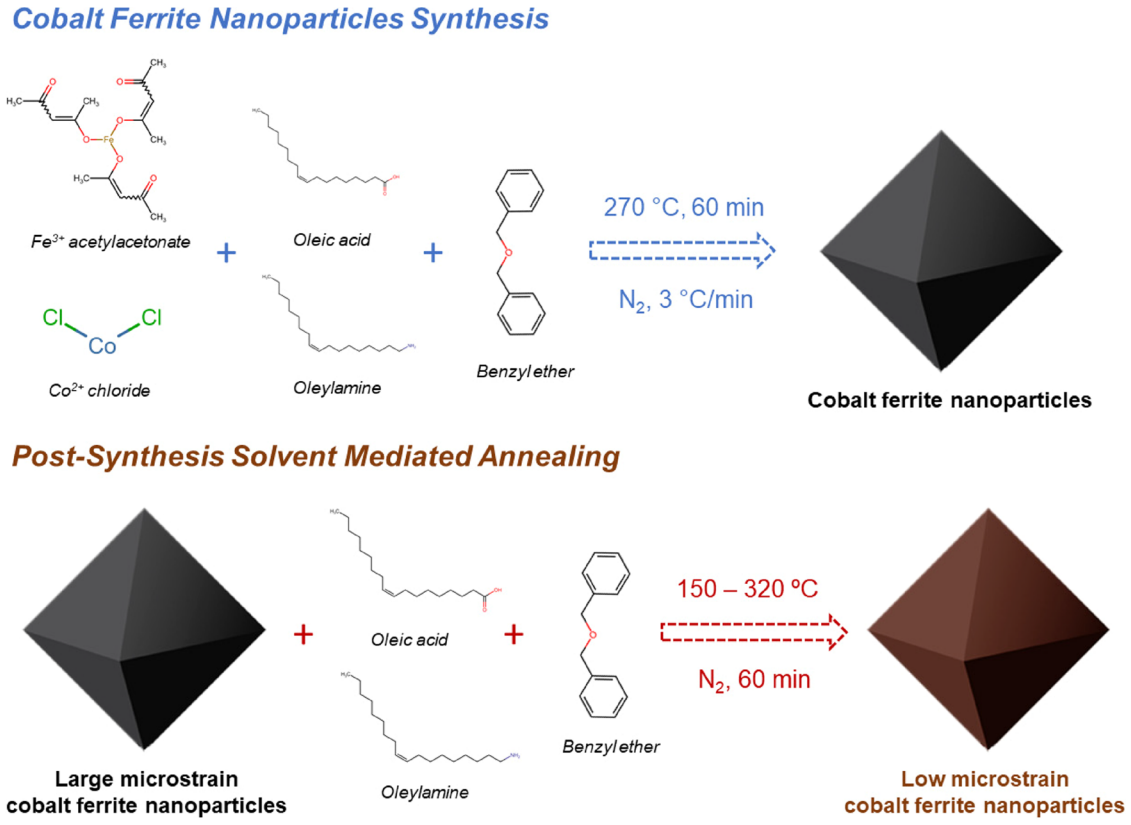

pristine sample. The effect was found to be maximum at 210 °C. The treatment at higher temperature (T > 300 °C), in fact, modifies the cationic homogeneity in the NPs, decreasing the cell parameter, with a consequent enhancement of the strain.

Furthermore, it has been shown that the medium where the annealing process occurs is essential to control the final properties of the NPs: in the classical annealing procedure performed on a dried powder, the stability of the organic layer surrounding the NPs does not allow the release of the lattice stress accumulated in the NPs, leading to the reduction of the initial coercivity; on the contrary, the solvent mediated treatment resulted in a long-range ordered crystal structure. It should be emphasized that the proposed post-treatment procedure can be envisaged to improve the magnetic properties of a broad range of nanomaterials, as, for example, soft ferrites, whose magnetic properties are critically strain-dependent.

On the other hand, this work reminds us that magnetic NPs should be always considered as metastable structures, which, being thermodynamically less favored than the corresponding micro and macrosized materials, naturally evolve during each postsynthesis treatment. Therefore, care must be taken whenever the magnetic behavior of complex multicomponent nanoheterostructures, obtained by multistep procedures, is interpreted in terms of the interaction among the component, without properly considering the possible transformation of each individual part.

■ EXPERIMENTAL SECTION

Chemicals and Materials. The synthesis was carried out using standard airless procedures and commercially available reagents: Benzyl ether (99%), 1-octadecene (90%), oleic acid (OA, 90%), oleylamine (OAm, >70%), iron(III) acetylacetonate ($Fe(acac)_3$, 99%), and cobalt(II) chloride anhydrous ($CoCl_2$, ≥99%). All starting materials were purchased from Sigma-Aldrich and used without further purification. $CoCl_2$ anhydrous was stored inside a glove box.

Synthesis of Cobalt Ferrite NPs (CFO). Cobalt ferrite NPs (**CFO**) were synthesized by dissolving 2 mmol of $Fe(acac)_3$, 1 mmol of $CoCl_2$, 6 mmol of OA, and 6 mmol of OAm in 25 mL of benzyl ether in a 50 mL three-neck round bottomed flask (Scheme 1). Initially, the mixture was degassed bubbling N_2 at 100 °C for 60 min, and then it was heated up to 270 °C for 60 min with a heating rate of 3 °C/min. During the heating and digestion process, the mixture was exposed to an N_2 flow. Finally, the flask was removed from the heating mantle and allowed cooling down under an inert atmosphere. The NPs were washed by several cycles of coagulation with ethanol, centrifugation at 5000 rpm, disposal of supernatant solution, and re-dispersion in hexane.

Solvent-Mediated Annealing Treatment of CFO. Afterward, **CFO** NPs were subjected to further heating process at different temperatures following a procedure commonly used for the growth of a ferrite shell.[8] 0.025 g of as-prepared NPs were re-dispersed in a solution containing 0.6 mmol of OA, 0.6 mmol of OAm, and 40 mL of benzyl ether or 1-octadecene in a 100 mL three-neck round bottomed flask. The mixture was degassed bubbling N_2 at 100 °C for 60 min, and then it was heated up to the desired temperature (150, 210, 270, or 320 °C) for 60 min with a heating rate of 3 °C/min. During the heating process, the mixture was exposed to a N_2 flow. Finally, the flask was removed from the heating mantle and allowed cooling down under an inert atmosphere. The NPs were washed by several cycles of coagulation with ethanol, centrifugation at 5000 rpm, disposal of supernatant solution, and re-dispersion in hexane. In addition, 0.025 g of **CFO** in powder was heated at 3 °C/min up to 210 °C under an N_2 atmosphere in an oven. The sample was kept at this temperature for 60 min and then cooled down to room temperature.

https://doi.org/10.1021/acsanm.2c03161
ACS Appl. Nano Mater. 2022, 5, 14871−14881

Structural, Morphological, and Chemical Composition Characterization. TEM images were obtained using a Philips CM12 microscope with a LaB_6 filament operated at 100 kV. The NPs were dispersed in hexane and then placed dropwise onto a holey carbon supported grid. The particle size of the different samples and the standard deviation were obtained by calculating the number average by manually measuring the equivalent edge length of >200 octahedral particles from TEM micrographs. Ultrahigh-resolution TEM (UHRTEM) images were acquired at 200 kV on a JEOL JEM-2200FS equipped with a Ω-filter (point resolution 0.19 nm). GPA was performed with the FRWRtools plugin for Digital Micrograph (Gatan, Inc.) on **CFO** and **CFO210** by analyzing 10−15 NPs.[61] The structure of the NPs was investigated by powder X-ray diffraction (XRD) using a Bruker New D8 ADVANCE ECO diffractometer equipped with Cu Kα radiation. The measurements were carried out in the range of 20−90°, with a step size of 0.01° and a collection time of 1 s. Quantitative analysis of the XRD data was undertaken with a full pattern fitting procedure based on the Rietveld method using the MAUD program.[62] All the weighted profile *R*-factors (R_{WP}) obtained from Rietveld analysis are in the range between 0.082 and 0.091. The transition metal content (w/w) in NPs was assessed by using an EDXRF spectrometer Shimadzu EDX-7000.

Magnetic Measurements. The magnetic properties of the NPs were measured on tightly packed powder samples using a vibrating sample mode (VSM, Quantum Design PPMS) magnetometer with 9 T maximum field. The hysteresis loops were measured at increasing temperatures after field cooling the sample in 5 T from 380 to 5 K. Saturation magnetization has been calculated extrapolating the M vs 1/H at high fields and the effective cubic magnetic anisotropy using the expression $K_{eff} = H_C M_S/0.64$.[8]

^{57}Fe Mössbauer spectra were recorded using a ^{57}Co/Rh γ-ray source mounted on an electromagnetic transducer with a triangular velocity form, at 12 K in an 8 T field oriented in parallel to the γ-beam. For the analysis of Mössbauer spectra, the program "Mosfit" was used. The hyperfine structure was modeled by a least-squares fitting procedure involving Zeeman sextets composed of Lorentzian lines. To describe the broadening of lines, several magnetic subcomponents were considered where isomer shift, quadrupolar shift, linewidth, and effective field values were left free during the refinement and the intensities of intermediate lines (2, 5) as well; the ratio of intensities of external/internal lines being found systematically equal to 3. The isomer shift (IS) values were referred to α-Fe at 300 K. The samples consisted of a thin layer of about 40 mg of the powdered compound.

■ ASSOCIATED CONTENT

Supporting Information

The Supporting Information is available free of charge at https://pubs.acs.org/doi/10.1021/acsanm.2c03161.

Energy-dispersive X-ray fluorescence; high-resolution transmission electron microscopy; X-ray diffraction data; X-ray diffraction data; Mössbauer spectroscopy; magnetic characterization; and ΔM plots (PDF)

■ AUTHOR INFORMATION

Corresponding Authors

Claudio Sangregorio − *ICCOM−CNR, I-50019 Sesto Fiorentino, Italy; Department of Chemistry "U. Schiff", University of Florence and INSTM, I-50019 Sesto Fiorentino, Italy;* orcid.org/0000-0002-2655-3901; Email: csangregorio@iccom.cnr.it

Alberto López-Ortega − *Department of Chemistry "U. Schiff", University of Florence and INSTM, I-50019 Sesto Fiorentino, Italy; Departamento de Ciencias and Institute for Advanced Materials and Mathematics, Universidad Pública de Navarra, E-31006 Pamplona, Spain;* orcid.org/0000-0003-3440-4444; Email: lopezortega.alberto@gmail.com

Authors

Beatrice Muzzi − *Department of Biotechnology, Chemistry and Pharmacy, University of Siena 1240, I-53100 Siena, Italy; ICCOM−CNR, I-50019 Sesto Fiorentino, Italy; Department of Chemistry "U. Schiff", University of Florence and INSTM, I-50019 Sesto Fiorentino, Italy;* orcid.org/0000-0001-9151-7723

Elisabetta Lottini − *Department of Chemistry "U. Schiff", University of Florence and INSTM, I-50019 Sesto Fiorentino, Italy*

Nader Yaacoub − *IMMM, Université du Mans, F-72085 Le Mans, France*

Davide Peddis − *Department of Chemistry and Industrial Chemistry, University of Genoa, I-16146 Genova, Italy; ISM−CNR, I-00015 Monterotondo Scalo, Italy;* orcid.org/0000-0003-0810-8860

Giovanni Bertoni − *CNR−Istituto Nanoscienze, I-41125 Modena, Italy;* orcid.org/0000-0001-6424-9102

César de Julián Fernández − *IMEM−CNR, I-43124 Parma, Italy;* orcid.org/0000-0002-6671-2743

Complete contact information is available at: https://pubs.acs.org/10.1021/acsanm.2c03161

Author Contributions

E.L., B.M., and A.L.O. performed the synthesis and the structural and magnetic characterization; B.M. and G.B. performed the TEM measurements; N.Y. and D.P. performed Mossbauer measurements. C.J.F., C.S., B.M., and A.L.O. conceived the experiments and wrote the paper which was critically revised by all the authors; all authors contributed to the discussions.

Funding

Open access funding provided by Universidad Pública de Navarra.

Notes

The authors declare no competing financial interest.

■ ACKNOWLEDGMENTS

This work was supported by EU-H2020 AMPHIBIAN Project (Grant no. 720853). A.L.O. acknowledges support from the Universidad Pública de Navarra (Grant no. PJUPNA2020).

■ REFERENCES

(1) Salata, O. V. Applications of Nanoparticles in Biology and Medicine. *J. Nanobiotechnol.* **2004**, *2*, 3.

(2) Reiss, G.; Hütten, A. Magnetic Nanoparticles: Applications beyond Data Storage. *Nat. Mater.* **2005**, *4*, 725−726.

(3) Papaefthymiou, G. C. Nanoparticle Magnetism. *Nano Today* **2009**, *4*, 438−447.

(4) López-Ortega, A.; Takahashi, M.; Maenosono, S.; Vavassori, P. Plasmon Induced Magneto-Optical Enhancement in Metallic Ag/FeCo Core/Shell Nanoparticles Synthesized by Colloidal Chemistry. *Nanoscale* **2018**, *10*, 18672−18679.

(5) Fantechi, E.; Innocenti, C.; Zanardelli, M.; Fittipaldi, M.; Falvo, E.; Carbo, M.; Shullani, V.; Di Cesare Mannelli, L.; Ghelardini, C.; Ferretti, A. M.; Ponti, A.; Sangregorio, C.; Ceci, P. A Smart Platform for Hyperthermia Application in Cancer Treatment: Cobalt-Doped Ferrite Nanoparticles Mineralized in Human Ferritin Cages. *ACS Nano* **2014**, *8*, 4705−4719.

(6) Saura-Múzquiz, M.; Granados-Miralles, C.; Stingaciu, M.; Bøjesen, E. D.; Li, Q.; Song, J.; Dong, M.; Eikeland, E.; Christensen, M. Improved Performance of $SrFe_{12}O_{19}$ Bulk Magnets through Bottom-up Nanostructuring. *Nanoscale* **2016**, *8*, 2857−2866.

(7) de Julián Fernández, C.; Sangregorio, C.; de la Figuera, J.; Belec, B.; Makovec, D.; Quesada, A. Progress and Prospects of Hard Hexaferrites for Permanent Magnet Applications. *J. Phys. D: Appl. Phys.* **2021**, *54*, 153001.
(8) López-Ortega, A.; Lottini, E.; de Julián Fernández, C.; Sangregorio, C. Exploring the Magnetic Properties of Cobalt-Ferrite Nanoparticles for the Development of a Rare-Earth-Free Permanent Magnet. *Chem. Mater.* **2015**, *27*, 4048−4056.
(9) Almessiere, M. A.; Trukhanov, A. V.; Slimani, Y.; You, K. Y.; Trukhanov, S. V.; Trukhanova, E. L.; Esa, F.; Sadaqati, A.; Chaudhary, K.; Zdorovets, M.; Baykal, A. Correlation Between Composition and Electrodynamics Properties in Nanocomposites Based on Hard/Soft Ferrimagnetics with Strong Exchange Coupling. *Nanomaterials* **2019**, *9*, 202.
(10) López-Ortega, A.; Estrader, M.; Salazar-Alvarez, G.; Roca, A. G.; Nogués, J. Applications of Exchange Coupled Bi-Magnetic Hard/Soft and Soft/Hard Magnetic Core/Shell Nanoparticles. *Phys. Rep.* **2015**, *553*, 1−32.
(11) Batlle, X.; Labarta, A. Finite-Size Effects in Fine Particles: Magnetic and Transport Properties. *J. Phys. D: Appl. Phys.* **2002**, *35*, 201.
(12) Knobel, M.; Nunes, W. C.; Socolovsky, L. M.; De Biasi, E.; Vargas, J. M.; Denardin, J. C. Superparamagnetism and Other Magnetic Features in Granular Materials: A Review on Ideal and Real Systems. *J. Nanosci. Nanotechnol.* **2008**, *8*, 2836−2857.
(13) Prado, Y.; Daffé, N.; Michel, A.; Georgelin, T.; Yaacoub, N.; Greneche, J. M.; Choueikani, F.; Otero, E.; Ohresser, P.; Arrio, M. A.; Cartier-dit-Moulin, C.; Sainctavit, P.; Fleury, B.; Dupuis, V.; Jerome, F. Enhancing the Magnetic Anisotropy of Maghemite Nanoparticles via the Surface Coordination of Molecular Complexes. *Nat. Commun.* **2015**, *6*, 10139.
(14) Vestal, C. R.; Zhang, Z. J. Effects of Surface Coordination Chemistry on the Magnetic Properties of MnFe2O4 Spinel Ferrite Nanoparticles. *J. Am. Chem. Soc.* **2003**, *10*, 9828−9833.
(15) Vasilakaki, M.; Ntallis, N.; Trohidou, K. N.; Yaacou, N.; Muscas, G.; Peddis, D.; Trohidou, K. N. Optimising the Magnetic Performance of Co Ferrite Nanoparticles via Organic Ligand Capping. *Nanoscale* **2018**, 21244−21253.
(16) Lee, J.; Jang, J.; Choi, J.; Moon, S. H.; Noh, S.; Kim, J.; Kim, J.-G.; Kim, I.-S.; Park, K. I.; Cheon, J. Exchange-Coupled Magnetic Nanoparticles for Efficient Heat Induction. *Nat. Nanotechnol.* **2011**, *6*, 418−422.
(17) Noh, S. H.; Na, W.; Jang, J. T.; Lee, J. H.; Lee, E. J.; Moon, S. H.; Lim, Y.; Shin, J. S.; Cheon, J. Nanoscale Magnetism Control via Surface and Exchange Anisotropy for Optimized Ferrimagnetic Hysteresis. *Nano Lett.* **2012**, *12*, 3716−3721.
(18) Cannas, S. C.; Vejpravova, J.; Angotzi, M. S.; Mameli, V.; Cara, C.; Musinu, A.; Sangregorio, C.; Niznansky, D.; Xin, H. L.; Cannas, C. Coupled Hard−Soft Spinel Ferrite-Based Core−Shell Nanoarchitectures: Magnetic Properties and Heating Abilities. *Nanoscale Adv.* **2020**, *2*, 3191−3201.
(19) Lak, A.; Disch, S.; Bender, P. Embracing Defects and Disorder in Magnetic Nanoparticles. *Adv. Sci.* **2021**, No. 2002682.
(20) Lak, A.; Cassani, M.; Mai, B. T.; Winckelmans, N.; Cabrera, D.; Sadrollahi, E.; Marras, S.; Remmer, H.; Fiorito, S.; Cremades-jimeno, L.; Litterst, F. J.; Ludwig, F.; Manna, L.; Teran, F. J.; Bals, S.; Pellegrino, T. Fe^{2+} Deficiencies, FeO Sub-Domains, and Structural Defects Favor Magnetic Hyperthermia Performance of Iron Oxide Nanocubes into Intracellular Environment. *Nano Lett.* **2018**, *18*, 6856−6866.
(21) López-Ortega, A.; Lottini, E.; Bertoni, G.; De Julián Fernández, C.; Sangregorio, C. Topotaxial Phase Transformation in Cobalt Doped Iron Oxide Core/Shell Hard Magnetic Nanoparticles. *Chem. Mater.* **2017**, *29*, 1279−1289.
(22) Osborn, J.; Preface, A. Proceedings of the Fifth Symposium on Magnetism and Magnetic Materials, November 1959, Detroit, Michigan. *J. Appl. Phys.* **1960**, *1*, 1959−1961.
(23) Vázquez-Vázquez, C.; López-Quintela, M. A.; Buján-Núñez, M. C.; Rivas, J. Finite Size and Surface Effects on the Magnetic Properties of Cobalt Ferrite Nanoparticles. *J. Nanopart. Res.* **2011**, *13*, 1663−1676.
(24) Lappas, A.; Antonaropoulos, G.; Brintakis, K.; Vasilakaki, M.; Trohidou, K. N.; Iannotti, V.; Ausanio, G.; Kostopoulou, A.; Abeykoon, M.; Robinson, I. K.; Bozin, E. S. Vacancy-Driven Noncubic Local Structure and Magnetic Anisotropy Tailoring in Fe_xO-$Fe_{3-\delta}O_4$ Nanocrystals. *Phys. Rev. X* **2019**, *9*, 1−17.
(25) Bozorth, R. M.; Walker, J. G. Magnetostriction of Single Crystals of Cobalt and Nickel Ferrites. *Phys. Rev.* **1952**, *88*, 1209.
(26) Tachiki, M. Origin of the Magnetic Anisotropy Energy of Cobalt Ferrite. *Prog. Theor. Phys.* **1960**, *23*, 1055−1072.
(27) Thanh, N. T. K.; Maclean, N.; Mahiddine, S. Mechanisms of Nucleation and Growth of Nanoparticles in Solution. *Chem. Rev.* **2014**, *114*, 7610−7630.
(28) Verbeeck, J.; Bertoni, G. Model-Based Quantification of EELS Spectra: Treating the Effect of Correlated Noise. *Ultramicroscopy* **2008**, *108*, 74−83.
(29) Fantechi, E.; Campo, G.; Carta, D.; Corrias, A.; De Julián Fernández, C.; Gatteschi, D.; Innocenti, C.; Pineider, F.; Rugi, F.; Sangregorio, C. Exploring the Effect of Co Doping in Fine Maghemite Nanoparticles. *J. Phys. Chem. C* **2012**, *116*, 8261−8270.
(30) Qin, W.; Nagase, T.; Umakoshi, Y.; Szpunar, J. A. Relationship between Microstrain and Lattice Parameter Change in Nanocrystalline Materials. *Philos. Mag. Lett.* **2008**, *88*, 169−179.
(31) Zhang, Q.; Peng, X.; Nie, Y.; Zheng, Q.; Shangguan, J.; Zhu, C.; Bustillo, K. C.; Ercius, P.; Wang, L.; Limmer, D. T.; Zheng, H. Defect-Mediated Ripening of Core-Shell Nanostructures. *Nat. Commun.* **2022**, *13*, 1−10.
(32) Barker, A. J.; Cage, B.; Russek, S.; Stoldt, C. R. Ripening during Magnetite Nanoparticle Synthesis: Resulting Interfacial Defects and Magnetic Properties. *J. Appl. Phys.* **2005**, *98*, No. 063528.
(33) Hÿtch, M. J.; Snoeck, E.; Kilaas, R. Quantitative Measurement of Displacement and Strain Fields from HREM Micrographs. *Ultramicroscopy* **1998**, *74*, 131−146.
(34) Peddis, D.; Yaacoub, N.; Ferretti, M.; Martinelli, A.; Piccaluga, G.; Musinu, A.; Cannas, C.; Navarra, G.; Greneche, J. M.; Fiorani, D. Cationic Distribution and Spin Canting in CoFe2O4 Nanoparticles. *J. Phys.: Condens. Matter* **2011**, *23*, No. 426004.
(35) Santoyo Salazar, J.; Perez, L.; de Abril, O.; Truong Phuoc, L.; Ihiawakrim, D.; Vazquez, M.; Greneche, J.-M.; Begin-Colin, S.; Pourroy, G. Magnetic Iron Oxide Nanoparticles in 10-40 Nm Range: Composition in Terms of Magnetite/Maghemite Ratio and Effect on the Magnetic Properties. *Chem. Mater.* **2011**, *23*, 1379−1386.
(36) Artus, M.; Ben Tahar, L.; Herbst, F.; Smiri, L.; Villain, F.; Yaacoub, N.; Grenèche, J. M.; Ammar, S.; Fiévet, F. Size-Dependent Magnetic Properties of $CoFe_2O_4$ Nanoparticles Prepared in Polyol. *J. Phys.: Condens. Matter* **2011**, *23*, No. 506001.
(37) Concas, G.; Spano, G.; Cannas, C.; Musinu, A.; Peddis, D.; Piccaluga, G.; Musinu, A.; Peddis, D.; Piccaluga, G. Inversion Degree and Saturation Magnetization of Different Nanocrystalline Cobalt Ferrites. *J. Magn. Magn. Mater.* **2009**, *321*, 1893−1897.
(38) Cannas, C.; Musinu, A.; Piccaluga, G.; Fiorani, D.; Peddis, D.; Rasmussen, H. K.; Mørup, S. Magnetic Properties of Cobalt Ferrite-Silica Nanocomposites Prepared by a Sol-Gel Autocombustion Technique. *J. Chem. Phys.* **2006**, *125*, 164714.
(39) Peddis, D.; Mansilla, M. V.; Mørup, S.; Cannas, C.; Musinu, A.; Piccaluga, G.; Orazio, F. D.; Lucari, F.; Fiorani, D. Spin-Canting and Magnetic Anisotropy in Ultrasmall $CoFe_2O_4$ Nanoparticles. *J. Phys. Chem. B* **2008**, *112*, 8507−8513.
(40) Coey, J. M. D. Non-Collinear Spin Arrangement in Ultrafine Ferrimagnetic Crystallites. *Phys. Rev. Lett.* **1971**, *27*, 1140.
(41) Pedrosa, F. J.; Rial, J.; Golasinski, K. M.; Guzik, M. N.; Quesada, A.; Fernández, J. F.; Deledda, S.; Camarero, J.; Bollero, A. Towards High Performance $CoFe_2O_4$ Isotropic Nanocrystalline Powder for Permanent Magnet Applications. *Appl. Phys. Lett.* **2016**, *109*, 223105.
(42) Ponce, A. S.; Chagas, E. F.; Prado, R. J.; Fernandes, C. H. M.; Terezo, A. J.; Baggio-Saitovitch, E. High Coercivity Induced by

https://doi.org/10.1021/acsanm.2c03161
ACS Appl. Nano Mater. 2022, 5, 14871−14881

Mechanical Milling in Cobalt Ferrite Powders. *J. Magn. Magn. Mater.* **2013**, *344*, 182−187.
(43) Zhang, L. Y.; Li, Z. W. Synthesis and Characterization of $SrFe_{12}O_{19}/CoFe_2O_4$ Nanocomposites with Core-Shell Structure. *J. Alloys Compd.* **2009**, *469*, 422−426.
(44) Liu, B. H.; Ding, J. Strain-Induced High Coercivity in CoFe2O4 Powders. *Appl. Phys. Lett.* **2006**, *88*, No. 042506.
(45) Skomski, R. Nanomagnetics. *J. Phys.: Condens. Matter* **2003**, *15*, R841−R896.
(46) Chikazumi, S.*Physics of Ferromagnetism*; OUP Oxford, 2009.
(47) Lee, E. W. Magnetostriction and Magnetomechanical Effects. *Rep. Prog. Phys.* **1955**, *18*, 184−229.
(48) Klapel, G. D.; Shive, P. N. High-Temperature Magnetostrictionof Magnetite. *J. Geophys. Res.* **1974**, *79*, 2629−2633.
(49) Bozorth, R. M.; Walker, J. G. Magnetostriction of Single Crystals of Cobalt Ond Nickel Ferrites. *Phys. Rev.* **1952**, *88*, 1209.
(50) Kriegisch, M. Magnetic and Magnetoelastic Properties of Cobalt Ferrite. *J. Appl. Phys.* **2007**, *102*, No. 073910.
(51) Cullity, B. D.; Graham, C. D.*Introduction to Magnetic Materials*; Wiley, 2009.
(52) Dennis, C. L.; Ivkov, R.Physics of Heat Generation Using Magnetic Nanoparticles for Hyperthermia. 2013, *6736*, 1−15, .
(53) Carrey, J.; Mehdaoui, B.; Respaud, M. Simple Models for Dynamic Hysteresis Loop Calculations of Magnetic Single-Domain Nanoparticles: Application to Magnetic Hyperthermia Optimization. *J. Appl. Phys.* **2011**, *2011*, No. 083921.
(54) Dutz, S.; Hergt, R.; Mu, J.; To, J. Hysteresis Losses of Magnetic Nanoparticle Powders in the Single Domain Size Range. *J. Magn. Magn. Mater.* **2007**, *308*, 305−312.
(55) Lartigue, L.; Innocenti, C.; Kalaivani, T.; Awwad, A.; Sanchez, M.; Guari, Y.; Larionova, J.; Gu, C.; Montero, J. G.; Arosio, P.; Lascialfari, A.; Gatteschi, D.; Sangregorio, C.; Firenze, S. F. Water-Dispersible Sugar-Coated Iron Oxide Nanoparticles. An Evaluation of Their Relaxometric and Magnetic Hyperthermia Properties. *J. Am. Chem. Soc.* **2011**, *131*, 10459−10472.
(56) Yassine, S. R.; Fatfat, Z.; Darwish, G. H.; Karam, P. Catalysis Science & Technology of Magnetic Nanoparticles. *Catal. Sci. Technol.* **2020**, *10*, 3890−3896.
(57) Gyergyek, S.; Lisjak, D.; Beković, M.; Grilc, M.; Likozar, B.; Necemer, M.; Makovec, D. Magnetic Heating of Nanoparticles Applied in the Synthesis of a Magnetically Recyclable Hydrogenation Nanocatalyst. *Nanomaterials* **2020**, *10*, 1142.
(58) Wang, W. E. I.; Tuci, G.; Duong-viet, C.; Liu, Y.; Rossin, A.; Luconi, L. Induction Heating: An Enabling Technology for the Heat Management in Catalytic Processes. *ACS Catal.* **2019**, *9*, 7921−7935.
(59) Varsano, F.; Bellusci, M.; La, A.; Petrecca, M.; Albino, M.; Sangregorio, C. ScienceDirect Dry Reforming of Methane Powered by Magnetic Induction. *Int. J. Hydrogen Energy* **2019**, 21037−21044.
(60) Cosgrove, T.*Colloid Science: Principles, Methods and Applications*, 2nd ed.; Wiley2009.
(61) Useful Plugins and Scripts for DigitalMicrograph; Faculty of Mathematics and Natural Sciences, Department of Physics, Strukturforschung/Elektronenmikroskopie, 2016. https://www.physik.hu-berlin.de/en/sem/software/software_frwrtools.
(62) Lutterotti, L.*MAUD program*; 2016. http://www.ing.unitn.it/%7Emaud/.

https://doi.org/10.1021/acsanm.2c03161
ACS Appl. Nano Mater. 2022, 5, 14871−14881